Auger decay paths of mercury $5p$ and $4f$ vacancies revealed by multielectron spectroscopy

J. Palaudoux,[1,2,*] S.-M. Huttula,[1,2,3] M. Huttula,[1,2,3] F. Penent,[1,2] L. Andric,[1,2,4] and P. Lablanquie[1,2]

[1]*Laboratoire de Chimie Physique–Matière et Rayonnement, Université Pierre et Marie Curie,*
11 rue Pierre et Marie Curie, 75231 Paris Cedex 05, France

[2]*CNRS, Laboratoire de Chimie Physique–Matière et Rayonnement (UMR 7614),*
11 rue Pierre et Marie Curie, 75231 Paris Cedex 05, France

[3]*Department of Physics, MOMA-RC, P.O. Box 3000, 90014 University of Oulu, Finland*

[4]*Université Paris-Est, 5 boulevard Descartes, 77454 Marne-la-Vallée Cedex 2, France*

Single and double Auger processes following ionization of $4f$ and $5p$ inner shells have been studied using multielectron coincidence spectroscopy. Coincidence technique enables us to resolve state by state all single and double Auger paths with a resolution better than the lifetime broadening. Drastic step-to-step decay lifetime changes are observed and reported as Coster-Kronig transition takes place either in the first ($5p$) or in the second ($4f$) step of the Auger cascade. Relativistic *ab initio* theory has been used to predict and interpret the experimental observations.

PACS number(s): 32.30.−r, 32.80.Aa, 32.80.Hd, 31.15.A−

I. INTRODUCTION

Auger electron spectroscopy is a common tool to investigate the decay of atomic core-hole states and reveals detailed information about the electronic structure and the decay dynamics. In conventional noncoincident electron spectroscopy, an Auger spectrum typically results from superposition of transitions from several initial states to multiple final states. Often, additional complexity arises from the overlap of cascade processes. By implementing electron-electron coincidence techniques, the decay pathways can be resolved state by state. Several coincidence experiments appeared in the last decades (see, for example, [1–10]) and have proven their ability to disentangle the complexity of Auger spectra. In electron-electron coincidence experiments the photoelectron and one or several Auger electrons are detected together. Multielectron coincidences provide insight into the states (initial, intermediate, final) involved in the decay and a very efficient way to identify and interpret the pathways of the Auger decays.

Mercury is a liquid metal at room temperature with electronic configuration $[Kr]4d^{10}5s^24f^{14}5p^65d^{10}6s^2$. The $4f$ and $5p$ subshells have been previously studied by Svensson *et al.* [11]. The photoionization of the $4f$, $5d$, and $6s$ orbitals were further studied by Kobrin *et al.* [12] with the determinations of relative cross sections, branching ratios, and angular distributions of photoelectrons. The Auger decay of the $4f$ core hole leading to the $5d^{-2}$ final states was studied by Aksela *et al.* [13]. Lohman calculated the angular distribution and spin polarization of the Auger electrons [14,15] considering the population of $Hg^{2+} 5d^86s^2$ states. Recently, a detailed study of the $4f^{-1}V^{-1}$ core-valence double photoionization was reported by Huttula *et al.* [16]. The valence $6s$ and inner-valence $5d$ ionizations leading to singly and doubly ionized states of mercury were studied by Eland *et al.* [17] and the spectroscopy of the Hg^{3+} and Hg^{4+} states was reported by Huttula *et al.* [18].

In this paper, we present a detailed experimental study of single and double Auger processes following the creation of Hg^+ with $4f^{-1}$ and $5p^{-1}$ vacancies. The observations obtained with a magnetic bottle spectrometer [4] following inner-shell ionization by synchrotron radiation allow us to provide spin-orbit state selective spectra partially with subnatural linewidth resolution. The decay pathways are identified and we demonstrate clearly strong lifetime changes at the different steps of Auger cascade process observing a wide Coster-Kronig first-step transition ($5p$) followed by narrow linewidths of the second-step Auger. Conversely for the $4f$, the narrow and very intense first-step transition is followed by a wide Coster-Kronig transition. Relativistic *ab initio* multiconfiguration Dirac-Fock calculations are performed and presented to further interpret the experimental observations.

II. EXPERIMENTAL PROCEDURE

The experiments were carried out at the SOLEIL storage ring synchrotron radiation source in Saint Aubin (France). The magnetic bottle multielectron coincidence spectrometer, described in Ref. [4] was used at the PLEIADES beamline [19–23], which has two undulators HU256 and HU80 covering the 7–1000 eV energy range. The photon resolution was set at 65, 70, and 110 meV for the photon energies used to collect those data sets (175, 185, and 250 eV, respectively). Experiments were performed during single bunch operation mode [frequency $f \approx 850\,\text{kHz}$ ($T = 1.18\,\mu s$)] of the storage ring. Also, preliminary tests were carried out at BESSY II synchrotron in Berlin, Germany, with the same setup than the one described in this paper. Liquid Hg was evaporated to the gas phase using a resistively heated oven. A heated capillary needle was used to provide appropriate atomic mercury vapor density in the interaction region.

Electrons' time of flight (TOF) is measured by a time to digital converter (TDC) with a 250-ps resolution. The TDC acquisition procedure is initiated by the detection of a first electron, which opens a gate for 8 μs during which the arrival times of successive electrons and of the (delayed) ring pulse signal are measured. The electrons' TOF are determined as the

---

*jerome.palaudoux@upmc.fr

time difference between their arrival and the light pulse. Photon energy calibration of the monochromator was performed by measuring the total electron yield of He doubly excited states below the $He^+(N = 2)$ threshold, with the magnetic bottle. The TOF to kinetic energy calibration of the magnetic bottle was performed by measuring the $N = 2$ photoelectron satellite line of helium at number of kinetic energies starting from 200 meV. The helium $N = 1$ line was used for kinetic energies above 40 eV. The extrapolated position of zero kinetic energy electrons was also taken in account in the calibration. This calibration was cross checked with the positions of the double- ionized states of mercury, where the $5d^86s^2$ ($^1S_0$) state was taken to be at 48.90 eV binding energy [24]. Small energy shifts induced by different experimental conditions (e.g., deposition of mercury in the chamber inducing contact potentials) were corrected as constant energy shifts using a strong autoionization Auger line $5d_{3/2}^96p^2(^1S_0) \rightarrow 5d^{10}(^1S_0)$ of excited mercury atoms as an autocalibration point for low kinetic energy. See Ref. [18] for further details. The detection efficiency for electrons from 0 to 200 eV was found to be more than 55% allowing effective detection of 3 and 4 electrons in coincidence. In order to avoid any significant contribution of random coincidences, the electron count rate was limited to between 1 and 3 kHz. Thanks to the relatively long length of the TOF spectrometer (2.1 m), the energy resolution $\triangle E$ is found to be 10 meV for electron kinetic energies below 1 eV and $\triangle E/E = 1.6\%$ for higher kinetic energies.

III. CALCULATIONS

In order to analyze the experimental spectra, eigenenergies of the single-, double-, and triple-ionized states and intensities of the first-and second-step Auger processes were determined by using fully *ab initio* multiconfiguration Dirac-Fock method (MCDF). The MCDF method is described in detail elsewhere (see, e.g., [25] and references therein). GRASP92 program was used to solve the radial wave functions of the one-electron spin orbitals, and the atomic state functions (ASF) for bound states were obtained by diagonalizing the Hamiltonian matrix in the basis of JJ-coupled antisymmetric configuration state functions (CSF) with RCI program [25]. The radial wave functions were optimized by minimizing the average energy of the ASFs.

According to the two-step model of the Auger process, the number of emitted Auger electrons $n_{f\beta}$ in the first-step process from single-ionized state J_β to first-step Auger final state Jf is proportional to the product of the total ionization cross section and the relative Auger component rate

$$n_{f\beta} = \frac{2\pi \sum_{l_A j_A} \left| \sum_{\mu\nu} c_{f\mu} c_{\beta\nu} M_{f\beta}^{\mu\nu}(J_f, J_\beta) \right|^2}{P_\beta(J_\beta)} Q_\beta(J_\beta), \quad (1)$$

where $M_{f\beta}^{\mu\nu}(J_f, J_\beta)$ is the Coulomb matrix element $\langle \psi_\mu(J_f)\epsilon_A l_A j_A; J_\beta \| \sum_{mn}^{N-1} \frac{1}{r_{mn}} \| \psi_\nu(J_\beta) \rangle$, $P_\beta(J_\beta)$ is the total decay rate and $Q_\beta(J_\beta)$ is the $|\Psi(J_i)\rangle \rightarrow |\Psi(J_\beta)\rangle$. photoionization cross section.

For the second-step process, the final state of the first-step Auger process J_f decays to the triple-nized state J_q and the ionization cross section is replaced with the total population of Hg^{2+} state. The number of emitted second-step electrons

is then

$$n_{qf} = \frac{2\pi \sum_{l_B j_B} \left| \sum_{\mu\nu} c_{q\mu} c_{f\nu} M_{qf}^{\mu\nu}(J_q, J_f) \right|^2}{P_f(J_f)} \sum_i n_{f\beta(i)}, \quad (2)$$

and $\langle \psi_\mu(J_q)\epsilon_B l_B j_B; J_f \| \sum_{mn}^{N-1} \frac{1}{r_{mn}} \| \psi_\nu(J_f) \rangle$ is the corresponding Coulomb matrix element.

The Auger decay intensities were calculated using the AUGER component from the RATIP package. For more details about the AUGER program, see Refs. [26–28] and references therein.

IV. RESULTS AND DISCUSSION

The aim of this paper is to study the Auger decay following $5p$ and $4f$ inner-shell ionizations. To guide the discussion and predict the possible decay channels, the energy levels of single-, double-, and triple-ionized states are shown in Fig. 1. Experimental binding energies are taken from Svensson *et al.* [11] for Hg^+, from Eland *et al.* [17] and Huttula *et al.* [18] for Hg^{2+} and Hg^{3+} levels. The predicted binding energies of the Hg^{2+} states have been obtained by MC calculation including the nonrelativistic configurations $5d^{10}$, $5d^96s^1$, $5d^86s^2$, $5d^96p^1$, $5d^86p^2$, $5d^76s^26p^1$, $5d^76s^25f^1$, $5p^55d^{10}6s^1$, and $5p^55d^96s^2$. For the Hg^{3+} states, the MC calculation included nonrelativistic configurations $5d^9$, $5d^86s^1$, and $5d^76s^2$. The binding energies of the double- and triple-ionized states have been obtained as an energy difference to the eigenenergy of the mercury ground state. The predicted energy levels are shown in red (right side columns) in Fig. 1.

According to the calculations, both of the $5p^{-1}$ spin-orbit split ionized states may decay to the double-ionized states with $5d^{10}$, $5d^96s^1$, $5d^86s^2$ electronic configurations. These Hg^{2+} states lay in lower binding energies (35–50 eV) than Hg^{3+} ionization limit and thus they cannot decay further. In our calculations, the energy states belonging to the $5d^86p^2$ and
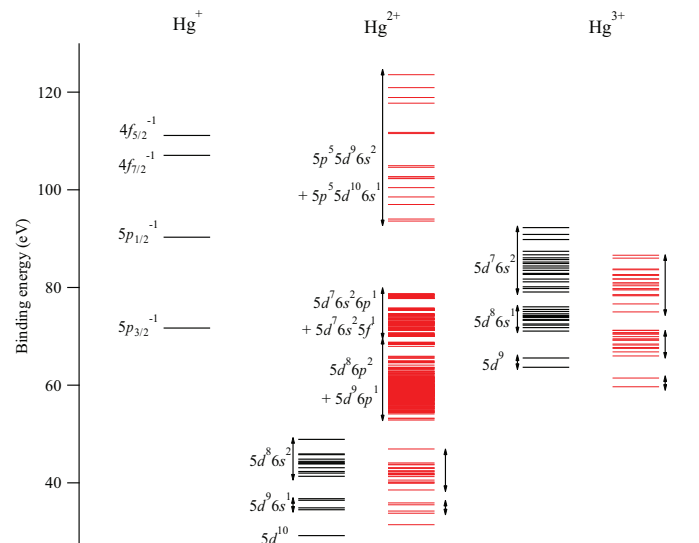

FIG. 1. (Color online) Energy-level diagram of atomic mercury. Hg^+, Hg^{2+}, and Hg^{3+} experimental binding energies (in black, left columns) are from literature [11,17,18], whereas our calculated values appear in red (right columns).

$5d^9 6p^1$ configurations (50–65 eV) lay close to the $5p_{3/2}^{-1}$ state whereas $5d^7 6s^2 5f^1$ and $5d^7 6s^2 6p^1$ configurations are energetically located mainly between the $5p_{3/2}^{-1}$ and $5p_{1/2}^{-1}$ states (65–80 eV). Thus, the Auger decay to these states is energetically possible only after $5p_{1/2}$ ionization. Our calculation included only the $5d^7 6s^2 6p^1$ and $5d^7 6s^2 5f^1$ configurations, but probably also other $5d^7 6s^2 nl-$type configurations exist in this binding energy region. The states related to Hg^{3+} $5d^7 6s^2$, $5d^8 6s^1$ and $5d^9$ configurations are located around 60–90 eV binding energies. Thus, the Hg^{3+} states can be populated after $5p$ ionization via $5d^8 6p^2 \rightarrow 5d^9$ and $5d^7 6s^2 nl-$type $\rightarrow$ $5d^8 6s^1$ paths.

The spin-orbit split $4f^{-1}$ states are located around 110 eV binding energy. In addition to the decay channels of the $5p^{-1}$ states, the $5p^5 5d^{10} 6s^1$ and $5p^5 5d^9 6s^2$ states may be populated after $4f$ ionization, and further decay to the Hg^{3+} $5d^7 6s^2$, $5d^8 6s^1$, and $5d^9$ states is possible. Detailed analysis of the decay paths is presented in Secs. IV A and IV B.

An experimental overview of the inner-shell ionization processes and the associated Auger decays is presented in Fig. 2. The photoelectron spectrum, displayed in bottom, shows the dominant spin-orbit splitted $4f$ photoelectrons peaks at a kinetic energy around 140 eV, $4f$ related satellite peaks at 130 eV, and two broad $5p$ photolines around 160 and 180 eV. The upper panel in Fig. 2 represents the energy correlation between all electron pairs detected in coincidence. Two intense vertical structures correspond to the detection of the $4f$ photoelectron in coincidence with the associated Auger electrons ranging from 0 to 75 eV. The weaker structure at 130 eV energy is associated to $4f$ satellites states, and their Auger decays can also be observed in the two-dimensional

map. The Auger decay of the $5p$ holes is observed in the coincidence map around 25 and 45 eV energies corresponding, respectively, to the decay of the $5p_{3/2}^{-1}$ and $5p_{1/2}^{-1}$ holes.

Diagonal lines indicate emission of two correlated electrons of constant energy sum; they correspond here to a double-photoionization (DPI) path populating a given Hg^{2+} final state. The most intense DPI line in the upper right part of the figure corresponds to the formation of unresolved Hg^{2+} $5d^8 6s^2$ states. The Auger decays of the $4f$ and $5p$ holes populate preferentially the Hg^{2+} $5d^8 6s^2$ states, but it is not the case for the Auger decay of the $4f$ satellite states. Finally, the weaker diagonal lines on the lower left corner of the two-dimensional map reveal the core-valence (CV) double-ionization path, which we have recently studied [16]. The horizontal line at Auger electron energy of $\sim$50–55 eV corresponds to the Auger electrons detected in coincidence with the faster photoelectron released in the CV double-ionization process.

A. Auger transitions following Hg^+ $5p^{-1}$ ionization

Both of the Hg^+ $5p_{3/2}$ and $5p_{1/2}$ states (at binding energies 71.7 and 90.3 eV [11]) lie above the Hg^{2+} $5d^8 6p^2$, $5d^9 6p^1$, $5d^8 6s^2$, $5d^9 6s^1$, and $5d^{10}$ doubly ionized states (see Fig. 1) and can undergo an Auger decay following:

$$Hg + h\nu \rightarrow Hg^+ 5p^{-1} + e_{ph}^- \rightarrow Hg^{2+} + e_{ph}^- + e_{Auger}^-. \quad (3)$$

The Auger spectra following selectively the $5p_{1/2}$ and $5p_{3/2}$ ionizations are presented in Fig. 3. To the best of our knowledge, the Auger decay of $5p$ holes has not been reported previously. The spectra have been obtained by selecting electron-electron coincidences e_{ph}^-, e_{Auger}^-), where a
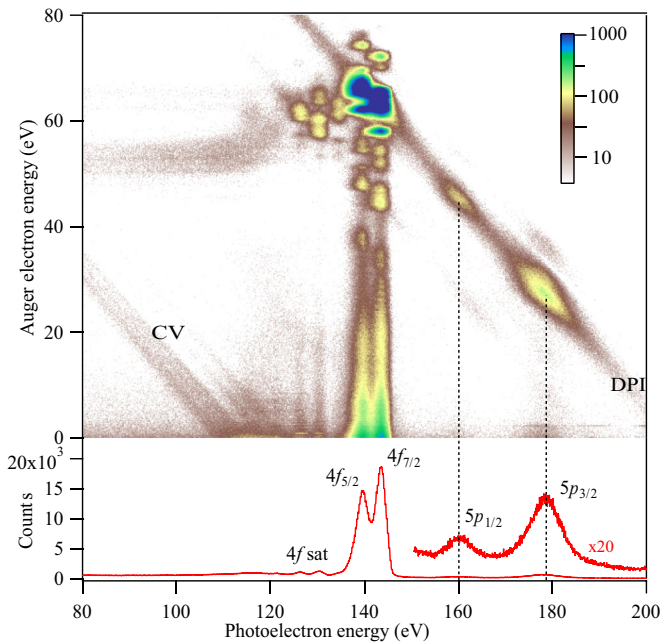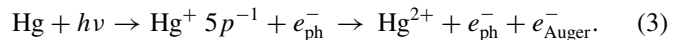

FIG. 2. (Color online) Bottom: Photoelectron spectrum showing the inner-shell ionization processes. Top: Two-dimensional presentation of the energy correlation between two electrons detected in coincidence. Counts (i.e., z axis in 2D picture) are given in logarithmic scale. Photon energy of 250 eV was used.
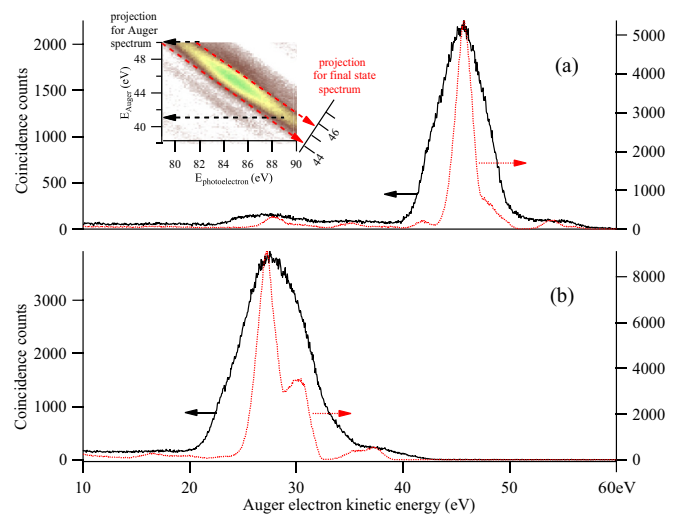

FIG. 3. (Color online) The Auger electrons detected in coincidence with (a) a $5p_{1/2}$ photoelectron and with (b) a $5p_{3/2}$ photoelectron. The coincidence counts are represented as a conventional Auger spectrum (solid curves) or as a selective population of the Hg^{2+} final states (red dashed curves), allowing one to cancel lifetime broadening. The inset depicts how the spectra are extracted by projection of the coincidence data set: on the vertical axis (conventional Auger spectrum) or along diagonal lines depicting Hg^{2+} final states. Photon energy of 175 eV was used.

$5p$ photoelectron e_{ph}^- has been detected, and by plotting the coincidence counts as a function of the kinetic energy E_{Auger} of the Auger electron. This way, the coincidence technique enables us to filter the Auger spectra associated with the decay of each ionized state. Note that in this method, the direct double-ionization path also contributes here; it is shown in Fig. 2 by the weak intensity along the diagonal line corresponding to DPI population of Hg^{2+} $5d^8 6s^2$ states, which lie under the $(5p, e_{Auger}^-)$ coincidence spots. It is, however, expected to be much weaker than the $5p$ resonant Auger decay.

The $5p^{-1}$ states have very short lifetimes due to their fast super Coster-Kronig decay to Hg^{2+} $5d^8 6s^2$ states, thus, both of the $5p$ photoelectron peaks (in Fig. 2) and the Auger peaks (in Fig. 3) are broad. Svensson *et al.* [11] measured a lifetime broadening of 6.2 eV for the $5p_{1/2}$ photoelectron line and of 5.6 eV for the $5p_{3/2}$ line, which are in agreement with our measurement. However, the coincidence technique makes it possible to go beyond this lifetime limitation and get a better resolution on the Hg^{2+} final states [29,30]. It is done by considering the population of the Hg^{2+} final states, which are defined by the sum of the kinetic energies of the Auger and the photoelectron [see Eq. (3) and the inset in Fig. 3]. This is known as the "subnatural linewidth Auger-photoelectron coincidence spectroscopy," and is demonstrated by plotting in Fig. 3 (red dashed line) the coincidence counts as a function of the variable $x = E_{photoelectron} + E_{Auger} - E^0_{photoelectron}$, where $E_{photoelectron}$ is the kinetic energy of each coincident $5p$ photo-electron and $E^0_{photoelectron}$ is the $5p$ nominal kinetic energy. The resulting spectrum does not include the lifetime broadening and corresponds to the selective population of the Hg^{2+} final states. Its resolution is purely experimental and fixed by the combined resolution of the Auger and the $5p$ photoelectron. Taking the analyzer resolution as $\Delta E/E = 1.6\%$, we estimate the resolution of the coincidence spectrum to be 1.5 eV or the $5p_{1/2}$ and 1.7 eV for the $5p_{3/2}$ spectrum.

The same coincidence spectra can be represented as a function of the binding energy by the relation $E_B(\text{Hg}^{2+}) = h\nu - E_{photoelectron} - E_{Auger}$. Experimental populations of the Hg^{2+} states are plotted in Fig. 4 together with the calculated ones. For computational reason, only the nonrelativistic configurations $5d^8 6p^2$, $5d^8 6s^2$, $5d^9 6s^1$, and $5d^{10}$ are included in the prediction, which changes also the predicted binding energies in Fig. 4 comparing to Fig. 1. Assignments and binding energies of the Hg^{2+} states are given in Table I together with the leading jj terms of the Hg^{2+} states. Also, the leading LS terms are given for the easier comparison with the previous studies [13,17], even if the Hg^{2+} states are, according to our calculation, nearly pure jj states.

The $5p$ Auger decay mainly populates Hg^{2+} $5d^8 6s^2$ states (super Coster-Kronig decay channel), whereas the doubly ionized ground state Hg^{2+} $(6s^0)$ is not populated. This is very similar to the equivalent decay of $4p$ hole in cadmium [31]. Although the experimental resolution does not allow resolving the individual Hg^{2+} final states, the agreement with theory is good. The inversion of the population of the two groups around 35 eV binding energy, consisting of states $5d_{3/2}^4 5d_{5/2}^5 6s^1$, $J = 2,3$ (left), and $5d_{3/2}^3 5d_{5/2}^4 6s^1$, $J = 1,2$ (right), is nicely reproduced by the theory. This indicates that the decay of the vacancy in the $5p_{1/2}$ subshell prefers to involve an electron
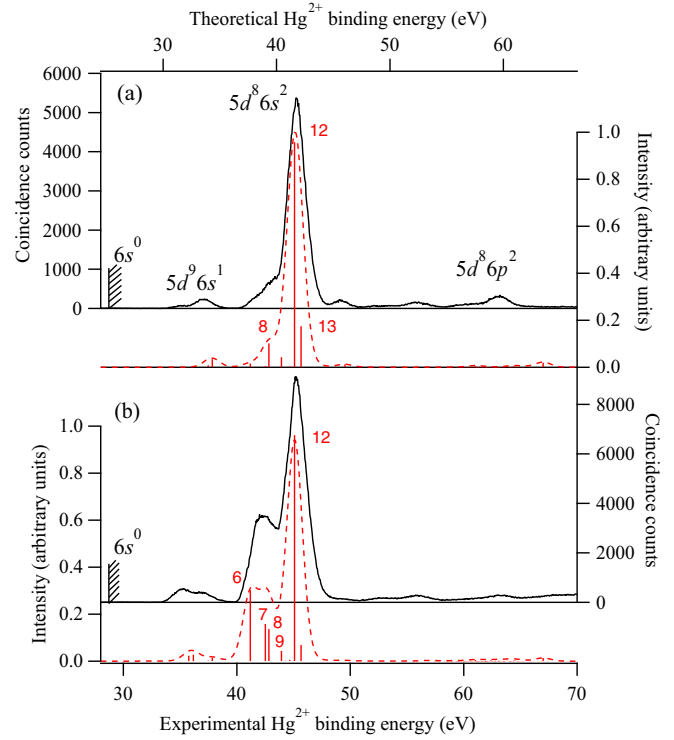

FIG. 4. (Color online) Experimental (solid black) and calculated (dashed red) populations of Hg^{2+} states after ionization of (a) $5p_{1/2}$ and (b) $5p_{3/2}$ subshells. The calculated curves have been convoluted with Gaussian profile of 1.5 eV width, which is an estimate of the experimental resolution (see text). The bars in the figure show the calculated binding energy positions and populations of the individual final states. For the line numbers, see Table I.

from $d_{3/2}$ subshell and the vacancy in the $5p_{3/2}$ subshell from $d_{5/2}$ subshell. The same trend is seen to give rise to the intense line at binding energy of 41.33 eV (experimental) in Fig. 4(b) (corresponding to the Hg^{2+} $5d_{3/2}^4 5d_{5/2}^4 6s^2$, $J = 4$ state) and to the weak line at binding energy of 48.9 eV (experimental) in Fig. 4(a) (corresponding the $5d_{3/2}^2 5d_{5/2}^6 6s^2$, $J = 0$ state).

Hg^{2+} states of binding energy above 50 eV are also weakly populated by the $5p$ Auger decay; theory predicts here the $5d^8 6p^2$ double-ionized states. According to our calculations, the $5d^7 6s^2 nl$ states are located around 80 eV binding energies and thus they are outside the energy region shown in Fig. 4.
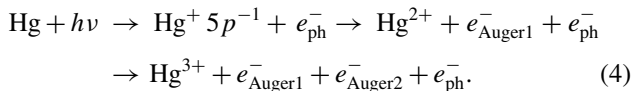
The double Auger path is open for both $5p_{1/2}$ and $5p_{3/2}$ vacancies as was discussed previously. Figure 5 shows a two-dimensional (2D) picture presenting the energy correlations between two Auger electrons detected in coincidence with a $5p_{1/2}$ photoelectron. The 2D map of the $5p_{3/2}$ subshell double Auger decay is not shown here since this subshell is lower in binding energy than the $5p_{1/2}$ and allows populating less Hg^{3+} states. Three broad diagonal lines in Fig. 5 correspond to the formation of unresolved Hg^{3+} final states of $5d^9$, $5d^8 6s^1$, and $5d^7 6s^2$ configurations.

As in other atomic double Auger processes [4,32], one can observe the contribution of direct and cascade paths. In the direct path, the two Auger electrons are emitted simultaneously and share continuously the excess energy, giving rise to intensity along the diagonal lines in Fig. 5. The cascade path

TABLE I. Experimental (Refs. [17] and [18]) and calculated binding energies, leading jj and LS terms of the Hg^{2+} states and their relative populations after $5p$ or $4f$ ionization.

	Hg^{2+} Binding Energy (in eV)			Hg^{2+} population after decay of (%)			
	This Calc.	Expt. (Refs. [17] or [18])	Assignment of Hg^{2+} state	$5p_{1/2}$	$5p_{3/2}$	$4f_{5/2}$	$4f_{7/2}$
1	29.508	29.19	$^1S_0 : 5d^{10} \, (J = 0)$	0.00	0.02	0.02	0.05
2	32.259	34.51	$^3D_3 : 5d_{3/2}^4 5d_{5/2}^5 \, (J = 5/2) \, 6s^1 \, (J = 3)$	0.00	1.32	0.10	1.06
3	32.672	34.90	$^3D_2 : 5d_{3/2}^4 5d_{5/2}^5 \, (J = 5/2) \, 6s^1 \, (J = 2)$	0.01	1.58	0.20	1.23
4	33.973	36.43	$^3D_1 : 5d_{3/2}^3 \, (J = 3/2) 5d_{5/2}^6 \, 6s^1 \, (J = 1)$	0.62	0.14	0.76	0.03
5	34.344	36.77	$^1D_2 : 5d_{3/2}^3 \, (J = 3/2) 5d_{5/2}^6 \, 6s^1 \, (J = 2)$	2.53	0.83	1.33	0.62
6	37.693	41.33	$^3F_4 : 5d_{3/2}^4 5d_{5/2}^4 \, (J = 4) \, 6s^2 \, (J = 4)$	1.17	17.21	2.30	15.35
7	39.017	42.34	$^3F_2 : 5d_{3/2}^4 5d_{5/2}^4 \, (J = 2) \, 6s^2 \, (J = 2)$	0.40	9.26	0.20	22.91
8	39.328	43.11	$^3F_3 : 5d_{3/2}^3 5d_{5/2}^5 \, (J = 3) \, 6s^2 \, (J = 3)$	7.50	7.80	8.76	6.73
9	40.428	43.94	$^3P_2 : 5d_{3/2}^3 5d_{5/2}^5 \, (J = 2) \, 6s^2 \, (J = 2)$	3.15	2.66	11.75	11.59
10	40.771	44.40	$^3P_0 : 5d_{3/2}^4 5d_{5/2}^4 \, (J = 0) \, 6s^2 \, (J = 0)$	0.01	0.15	0.55	7.47
11	41.168		$^3P_1 : 5d_{3/2}^3 5d_{5/2}^5 \, (J = 1) \, 6s^2 \, (J = 1)$	0.21	0.31	12.33	9.46
12	41.580	44.87	$^1G_4 : 5d_{3/2}^3 5d_{5/2}^5 \, (J = 4) \, 6s^2 \, (J = 4)$	70.66	54.66	16.04	13.28
13	42.168	45.77	$^1D_2 : 5d_{3/2}^2 (J = 2) \, 5d_{5/2}^6 \, 6s^2 \, (J = 2)$	12.84	3.94	28.71	3.14
14	46.027	48.90[18]	$^1S_0 : 5d_{3/2}^2 (J = 0) \, 5d_{5/2}^6 \, 6s^2 \, (J = 0)$	0.90	0.12	16.89	6.93

is the dominant one and corresponds to a sequential decay:

$$\mathrm{Hg} + h\nu \; \rightarrow \; \mathrm{Hg}^+ \, 5p^{-1} + e^-_{\mathrm{ph}} \; \rightarrow \; \mathrm{Hg}^{2+} + e^-_{\mathrm{Auger1}} + e^-_{\mathrm{ph}}$$

$$\rightarrow \; \mathrm{Hg}^{3+} + e^-_{\mathrm{Auger1}} + e^-_{\mathrm{Auger2}} + e^-_{\mathrm{ph}}. \qquad (4)$$

It gives rise in Fig. 5 to broad structures superimposed over the diagonal lines associated with Auger electron pairs of fixed energies.

In the same way as for the $5p$ single Auger spectra, the double Auger spectrum of Fig. 5 is affected by the short lifetime of the $5p_{1/2}$ hole with a lifetime broadening of 6.2 eV [11]. A close look at the cascade paths present in the $5d^9$ channel shows that it is the fast Auger electron peak, which is broad whereas the slow Auger electron peak is narrow. According to the calculations, the cascade process goes through the Hg^{2+} $5d^8 6p^2$ states with very fast super Coster-Kronig transition in the first step, whereas in the slower second-step decay the participating electrons are from the different subshell leading to $5d^9$ triple-ionized final states. The population of the $5d^8 6s^1$ final states originates from the same kind of cascade process. The first-step processes are fast
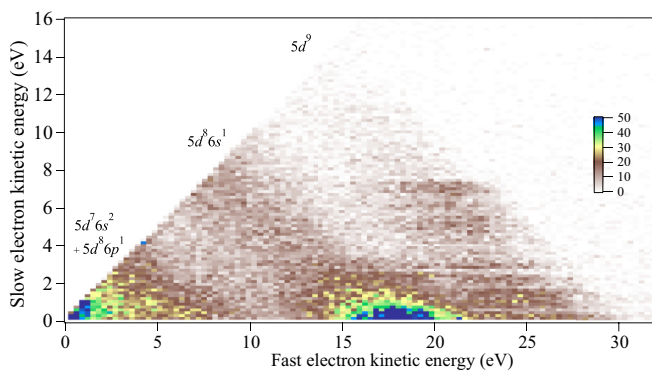
super Coster-Kronig transitions to the $5d^7 6s^2 nl$−type states (energy of the first-step Auger electron about 18 eV), which decay with slower Auger decay to $5d^8 6s^1$ state emitting very slow Auger electrons.

The experiment shows also an unexpectedly high population of the $5d^7 6s^2$ states after $5p_{1/2}$ ionization, even the obvious decay channel is missing. Thus, we have performed an additional calculation to see the location of $5d^8 6p^1$ configuration. The calculation reproduces the experimental energy region reported by Joshi [33]. The states are overlapping the $5d^7 6s^2$ region and may explain the population of the Hg^{3+} states at this binding energy region via decay channel $5p_{1/2}^{-1} \rightarrow 5d^7 6s^2 6p \rightarrow 5d^8 6p^1$. Although Ref. [18] demonstrates that these $5d^8 6p^1$ states are fully negligible in integrated population of the final states, here in identifying a selected route their population may be observed. Unfortunately, we are unable to confirm this reliably both in experiment and in theory. In contrast to the $5p_{1/2}$, the $5p_{3/2}$ state can decay only to the $5d^9$ and $5d^8 6s^1$ triply ionized states, as the decay to the $5d^7 6s^2$ states is not energetically possible.

The populations of the Hg^{3+} states through double Auger decay of the $5p$ vacancies are displayed in Fig. 6. In a similar way as for the single Auger decay, the lifetime broadening due to the short lifetime of the $5p$ holes is canceled out by considering the energy balance between the emitted photoelectron and two Auger electrons, and by writing energy conservation between initial and final states of the double Auger decay route:

$$E_B(\mathrm{Hg}^{3+}) = h\nu - E_{\mathrm{ph}} - E_{\mathrm{Auger1}} - E_{\mathrm{Auger2}} \qquad (5)$$

Considering only the sum of the kinetic energies of the two Auger electrons from Fig. 5, lifetime broadening would affect the obtained Hg^{3+} spectral widths. Now, the resolution of the final-state population in Fig. 6 is purely experimental; it is given by the combination of the resolution on each electron and is essentially affected by the energy resolution of the $5p$ photoelectron, which is here faster than the Auger electrons (at the photon energy of 175 eV the $5p_{3/2}$ and $5p_{1/2}$
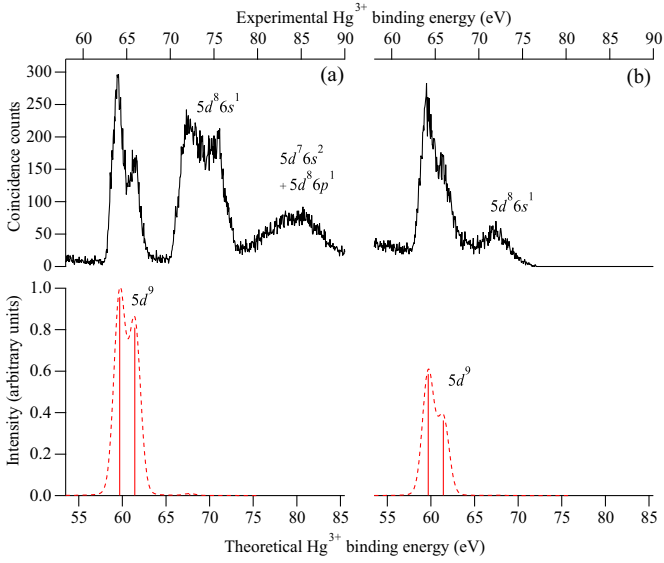

FIG. 5. (Color online) Energy correlations between two Auger electrons detected in coincidence with a $5p_{1/2}$ photoelectron. Counts (z axis in 2D picture) are given on a linear scale.

FIG. 6. (Color online) Experimental (top) and predicted (bottom) populations of Hg^{3+} states after (a) $5p_{1/2}$ and (b) $5p_{3/2}$ ionization. The photon energy is set at 175 eV. The calculated curves have been convoluted with Gaussian profile of 1.5 eV width, which is the estimated experimental resolution. The bars in the figure show the calculated binding energies and populations of the individual final states.
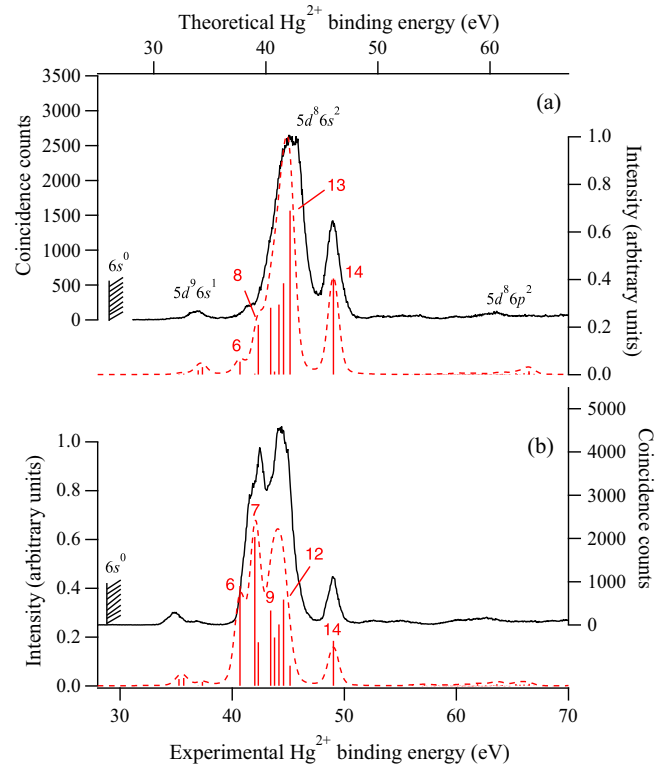

FIG. 7. (Color online) Experimental (solid black line) and calculated (dashed red line) populations of Hg^{2+} states by the Auger decay following (a) $4f_{5/2}$ and (b) $4f_{7/2}$ ionized states. The calculated curves have been convoluted with a Voigt profile (1 eV Gaussian and 0.24 eV Lorentzian components) to account for the experimental resolution. For the line numbers, see Table I.

photoelectrons have kinetic energies of 103.3 and 84.7 eV, respectively). The energy resolution is observed to be adequate to resolve individually the Hg^{3+} $5d^9$ states, being slightly worse in the case of $5p_{3/2}$ than in $5p_{1/2}$ (FWHM 1.7 versus 1.5 eV) due to the energy dependence of the resolution.

The bottom spectra in Fig. 6 show the predicted populations convoluted with the estimated experimental broadening of 1.5 eV. Because the $5d^7 6s^2 nl$ states are not included in the decay rate calculations, mainly the Hg^{3+} $5d^9$ are predicted to gain intensity via the cascade Auger decays through Hg^{2+} $5d^8 6p^2$ intermediate states. We expect that the double Auger process via $5d^7 6s^2 5f^1$ and $5d^7 6s^2 6p^1$ states is the main route to populate the states in binding energy range of $5d^8 6s^1$ and $5d^7 6s^2$ final states.

The multicoincidence experiment allows us to deduce the probability for double Auger decay of the $5p$ vacancies. This is done by comparing the number of events, in which a $5p$ photoelectron has been detected in coincidence with one or two Auger electrons. Taking into account the 60% detection efficiency, we obtain the double Auger probability of 25.0% and 6.5% for $5p_{1/2}$ and $5p_{3/2}$ decays, respectively. Due to the absence of the $5d^7 6s^2 nl$ configurations in the calculations, the theoretical probability of double Auger process after $5p$ ionization is not given.

B. Auger transition following Hg^+ $4f^{-1}$ ionization

The binding energies of the $4f_{7/2}{}^{-1}$ and $4f_{5/2}{}^{-1}$ ionized states are 107.06 and 111.13 eV, respectively [11]. Due to the absence of the Coster-Kronig process, the lifetimes of the states are more than one order of magnitude longer than for $5p^{-1}$ holes being 0.24 eV [13]. The experimental populations of the Hg^{2+} states by $4f$ single Auger decay are presented

in Fig. 7 together with the predictions. In spite of the limited experimental resolution, agreement with the theory is quite good. The experimental curves have been obtained as in Fig. 3 from the kinetic energies of the Auger electrons detected in coincidence with a $4f$ photoelectron. Photon energy of 185 eV is used in the measurement to separate the $4f$ components, and set the photoelectron faster than the Auger electrons. The spectrum in Fig. 7 is in principle affected by the $4f$ lifetime broadening (0.24 eV), but the limitation is here due to the experimental resolution ($\sim$1 eV) on the fast ($\sim$60 eV) Auger electrons. As in the case of the $5p$ Auger decay, Hg^{2+} $5d^8 6s^2$ are the main populated states. Similarly to the $5p$ decay, the doubly ionized state Hg^{2+} $6s^0$ is not populated by the Auger decay of the $4f$ vacancies. The inverted population of the two groups of Hg^{2+} $5d^9 6s^1$ states after selective photoionization of $4f_{5/2}$ and $4f_{7/2}$ is here well predicted by the theory. As in the case of the $5p$ ionization, an electron from $5d_{3/2}$ subshell prefers to fill hole in $4f_{5/2}$ subshell and an electron from $5d_{5/2}$ subshell prefers to fill hole in $4f_{7/2}$ subshell. This selection explains the inverted population of the two groups of Hg^{2+} $5d^9 6s^1$ states and also the higher population of the states around 41–42 eV binding energies (experimental) in $4f_{7/2}$ decay [Fig. 7(b)] in comparison to $4f_{5/2}$ [Fig. 7(a)]. Identifications and predicted populations of the Hg^{2+} states are given in Table I. The weak highly excited Hg^{2+} states of
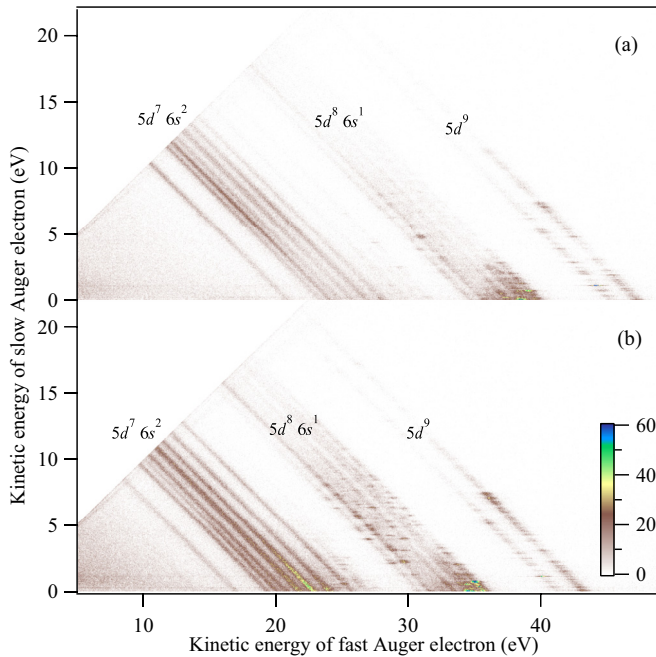
FIG. 8. (Color online) Energy correlation between two Auger electrons detected in coincidence with (a) $4f_{5/2}$ or (b) $4f_{7/2}$ photoelectron. Photon energy of 185 eV was used. Counts (z axis in 2D picture) are given on a linear scale.

FIG. 9. (Color online) The experimental (top) and predicted (bottom) populations of Hg^{3+} states after $4f_{5/2}$ (left) and $4f_{7/2}$ (right) ionization. The prediction has been convoluted with a Voigt profile (0.7 eV Gaussian and 0.24 eV Lorentzian components) to account for the experimental resolution. The bars represent the binding energies and intensities of the individual final states.

binding energy above 50 eV are assigned to states of $5d^8 6p^2$ configuration.

We consider now the decay of $4f$ holes by double Auger decay. Figure 8 shows the two-dimensional representation of the energy correlations between two Auger electrons detected in coincidence with a $4f_{5/2}$ and a $4f_{7/2}$ photoelectron. Three groups of diagonal lines are observed and correspond to the formation of Hg^{3+} final states belonging to the $5d^9$, $5d^8 6s^1$, and $5d^7 6s^2$ configurations. Compared to Fig. 5, one can observe that the Hg^{3+} states are now clearly resolved (for instance, the two Hg^{3+} $5d^9$ $^2D_{5/2}$ and $^2D_{3/2}$ states). In the same way as for the single Auger spectrum in Fig. 7, the resolution in Fig. 8 is now limited by the experimental resolution and not by the lifetime of the hole. As was observed in the case of $5p_{1/2}$, the $4f$ double Auger spectrum reveals the contribution of weak direct and dominant cascade paths.

Figure 9 shows the measured and predicted population of Hg^{3+} states ($5d^9$, $5d^8 6s^1$, and $5d^7 6s^2$ configurations) following the $4f_{5/2}$ and $4f_{7/2}$ double Auger decay. The experimental curves are obtained as summation of the 2D spectra along the $x = y$ diagonals whereas the predicted curves correspond to MCDF calculations based on the two-step model. The experimental broadening in Fig. 9 originates from the $4f$ lifetime broadening (0.24 eV) and from the combined experimental resolution of each Auger electron. The latter is hard to estimate precisely, but can be taken less than $\sim$0.7 eV, which is the resolution of the fastest possible Auger electron of 40–45 eV. Note that the $5d^7 6s^1 nl$ states are not included in the Auger rate calculations because of the very large number of the intermediate states, which makes the calculations complicated. The predicted population of the $5d^7 6s^2$ states corresponds quite well to the experiment. However, the populations of the
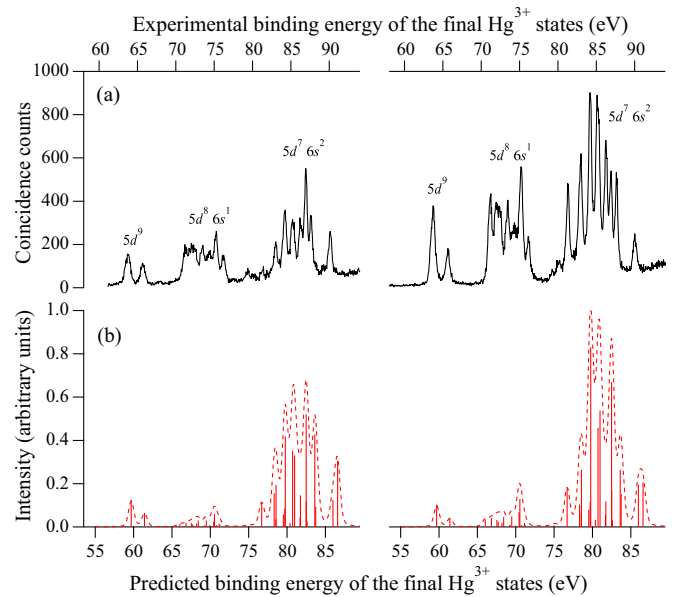
$5d^8 6s^1$ and $5d^9$ states are too weak compared to experiment due to the lack of the important $5d^7 6s^1 nl$ configurations in the calculations.

Figure 10 presents the one-dimensional double Auger spectra associated with the decay of a $4f_{5/2}$ and a $4f_{7/2}$ hole to Hg^{3+} final states of $5d^9$, $5d^8 6s^1$, and $5d^7 6s^2$ configurations. These spectra are deduced from the three-electron coincidence map
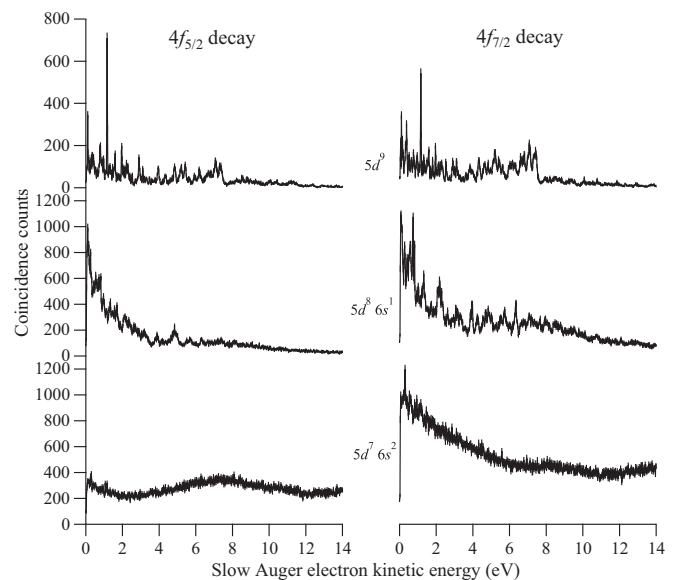

FIG. 10. Second-step Auger spectra associated with the decay of a $4f_{5/2}$ (left) or a $4f_{7/2}$ (right) vacancy to a specific Hg^{3+} final state (from top to bottom, $5d^9$, $5d^8 6s^1$, and $5d^7 6s^2$). The contribution of the direct double Auger was not substracted.

(Fig. 8) as horizontal projections for each final-state configuration separately. The spectra reveal different line structures related to Hg^{2+} intermediate states involved in the cascade double Auger decay. The sharp lines of the $5d^9$ and $5d^86s^1$ spectra suggest long-living Hg^{2+} intermediate states. In contrast, the broad structures of the Auger spectra at around 7 and 0 eV kinetic energies ($4f_{7/2}$ and $4f_{5/2}$, respectively) leading to the Hg^{3+} $5d^76s^2$ final-state configuration suggest the presence of cascade paths through short-lived Hg^{2+} intermediate state.

Our calculations suggest that the Hg^{2+} intermediate states involved in the $4f$ double Auger decay belong either to $5p^55d^96s^2$, $5p^55d^{10}6s^1$, $5d^76s^2nl-$type or $5d^86p^2$ configurations (see Fig. 1). Due to the presence of a $5p$ hole, the Hg^{2+} $5p^55d^96s^2$ and $5p^55d^{10}6s^1$ states decay preferentially by a very fast super-Coster-Kronig–type of Auger transitions, i.e., the Hg^{2+} $5p^55d^96s^2$ states decay to the $5d^76s^2$ triple-ionized states, and the Hg^{2+} $5p^55d^{10}6s^1$ states to Hg^{3+} $5d^86s^1$ states. This explains the broad bands observed for the $5d^76s^2$ and $5d^86s^1$ Hg^{3+} final states (see Figs. 8 and 10). The short lifetime of the Hg^{2+} $5p^55d^96s^2$ intermediate states can be expected to be of the same order of magnitude as that of the Hg^+ $5p$ hole, producing similar lifetime broadenings (~6 eV), which is indeed observed. The predicted probabilities of transitions from the $4f$ ionized state to the $5p^55d^96s^2$ intermediate state is much higher than to the $5p^55d^{10}6s^1$ states (intensity ratio about 18:1 after $4f_{7/2}$ ionization and 40:1 after $4f_{5/2}$ ionization) being in line with the visual observation in Fig. 8. The experimental intensity ratios for these transitions are unavailable as the coincidence map related to $5d^86s^1$ final-state configuration is dominated by sharp peaks associated with second-step Auger decays of Hg^{2+} $5d^76s^1nl$-type and $5d^86p^2$ intermediate states. However, the probability of the total $4f$ double Auger decays can be extracted. Taking into account the 60% detection efficiency, we obtain a probability of 32.0% and 30.5% for the $4f_{5/2}$ and $4f_{7/2}$ decays, respectively. One observes that the probabilty of double Auger decay increases with the excess energy of the $5p$ or $4f$ hole with respect to the Hg^{3+} threshold. Values of the same order of magnitude were reported for the $3d_{5/2}$ and $3d_{3/2}$ decays in Kr (respectively 28.4% and 29.1%) [32].

V. CONCLUSION

We have presented a detailed experimental and theoretical study of single and double Auger processes following the $4f^{-1}$ and $5p^{-1}$ vacancies in atomic mercury. Multicoincidence spectroscopy has allowed us to disentangle the Auger decay spin-orbit state selectively to each initial $4f_{7/2}$, $4f_{5/2}$, $5p_{3/2}$, and $5p_{1/2}$ hole. Relativistic *ab initio* multiconfiguration Dirac-Fock calculations were carried out to interpret the experimental observations and the related transition steps. The simulations of the processes were challenging due to the extremely high number of the Hg^{2+} states due to the several open atomic orbitals in the configurations. However, the calculations could nicely explain the experimental observations and provided understanding to the various decay routes leading to the population of Hg^{3+} states after photoionization of the $5p$ or $4f$ orbital.

The Auger decay spectra and the population of final states are provided by the pathways from the initial core-ionized states through the various Hg^{2+} intermediate states to the $5d^76s^2$, $5d^86s^1$, and $5d^9$ final-state configurations. We demonstrate the lifetime changes at the different steps of Auger cascade process observing a wide Coster-Kronig first-step transition ($5p$) followed by narrow linewidths for the second-step Auger. The study of the $5p$ decays shows the importance of the coincidence technique to go below the lifetime of the initial core-hole state and observe with a high resolution the Hg^{2+} and Hg^{3+} final states. An interesting process was observed for the $4f$ double Auger decay, in which a first Auger electron reflects the relatively long lifetime of the $4f$ vacancy, leading to an Hg^{2+} intermediate state with a $5p$ hole. In the second step, this Hg^{2+} intermediate state decays rapidly by emission of a second Auger electron similarly to the direct $5p$ Coster-Kronig decay. This sequence: slow emission of the first Auger electron, followed by fast emission of the second Auger electron is peculiar and reverse to what we observed in previous molecular [34] and atomic targets [4,7,32].

[1] P. Lablanquie, J. Delwiche, M. J. Franskin-Hubin, I. Nenner, J. H. D. Eland, and K. Ito, J. Mol. Struct. **174**, 141 (1988).

[2] Y. Hikosaka, R. I. Hall, F. Penent, P. Lablanquie, and K. Ito, Meas. Sci. Technol. **11**, 1697 (2000).

[3] J. Viefhaus, M. Braune, S. Korica, A. Reinköster, D. Rolles, and U. Becker, J. Phys. B: At., Mol. Opt. Phys. **38**, 3885 (2005).

[4] F. Penent, J. Palaudoux, P. Lablanquie, L. Andric, R. Feifel, and J. H. D. Eland, Phys. Rev. Lett. **95**, 083002 (2005).

[5] S. Sheinerman, P. Lablanquie, F. Penent, J. Palaudoux, J. H. D. Eland, T. Aoto, Y. Hikosaka, and K. Ito, J. Phys. B: At., Mol. Opt. Phys. **39**, 1017 (2006).

[6] Y. Hikosaka, T. Aoto, P. Lablanquie, F. Penent, E. Shigemasa, and K. Ito, J. Phys. B: At., Mol. Opt. Phys. **39**, 3457 (2006).

[7] P. Lablanquie, L. Andric. J. Palaudoux, U. Becker, M. Braune, J. Viefhaus, J. H. D. Eland, and F. Penent, J. Electron Spectrosc. Relat. Phenom. **156**, 51 (2007).

[8] Y. Hikosaka, P. Lablanquie, F. Penent, T. Kaneyasu, E. Shigemasa, J. H. D. Eland, T. Aoto, and K. Ito, Phys. Rev. A **76**, 032708 (2007).

[9] J. Palaudoux, P. Lablanquie, L. Andric, J. H. D. Eland, and F. Penent, J. Phys.: Conf. Ser. **141**, 012012 (2008).

[10] S. Ricz, Á. Kövér, M. Jurvansuu, D. Varga, J. Molnár, and S. Aksela, Phys. Rev. A **65**, 042707 (2002).

[11] S. Svensson, N. Mårtensson, E. Basilier, P. Å. Malmqvist, U. Gelius, and K. Siegbahn, J. Electron Spectrosc. **9**, 51 (1976).

[12] P. H. Kobrin, P. A. Heimann, H. G. Kerkhoff, D. W. Lindle, C. M. Truesdale, T. A. Ferrett, U. Becker, and D. A. Shirley, Phys. Rev. A **27**, 3031 (1983).

[13] H. Aksela, S. Aksela, J. S. Jen, and T. D. Thomas, Phys. Rev. A **15**, 985 (1977).

[14] B. Lohmann, J. Phys. B: At., Mol. Opt. Phys. **25**, 4163 (1992).

[15] B. Lohmann, J. Phys. B: At., Mol. Opti. Phys. **26**, 1623 (1993).

[16] M. Huttula, S.-M. Huttula, S. Fritzsche, P. Lablanquie, F. Penent, J. Palaudoux, and L. Andric, Phys. Rev. A **89**, 013411 (2014).

[17] J. H. D. Eland, R. Feifel, and D. Edvardsson, J. Phys. Chem. A **108**, 9721 (2004).

[18] M. Huttula, S.-M. Huttula, P. Lablanquie, J. Palaudoux, L. Andric, J. H. D. Eland, and F. Penent, Phys. Rev. A **83**, 032510 (2011).

[19] C. Miron *et al.*, http://www.synchrotron-soleil.fr/portal/page/portal/Recherche/LignesLumiere/PLEIADES

[20] O. Travnikova, J. C. Liu, A. Lindblad, C. Nicolas, J. Söderström, V. Kimberg, F. Gel'mukhanov, and C. Miron, Phys. Rev. Lett. **105**, 233001 (2010).

[21] J. Söderström, A. Lindblad, A. Grum Grzhimailo, O. Travnikova, C. Nicolas, S. Svensson, and C. Miron, New J. Phys. **13**, 073014 (2011).

[22] C. Miron, C. Nicolas, O. Travnikova, P. Morin, Y. P. Sun, F. Gel'mukhanov, N. Kosugi, and V. Kimberg, Nat. Phys. **8**, 135 (2012).

[23] A. Lindblad, V. Kimberg, J. Söderström, C. Nicolas, O. Travnikova, N. Kosugi, F. Gel'mukhanov, and C. Miron, New J. Phys. **14**, 113018 (2012).

[24] C. E. Moore, *Atomic Energy Levels*, US National Bureau of Standards, Vol. 1 (US Government Printing Office, Washington, DC, 1971).

[25] F. A. Parpia, C. F. Fischer, and I. P. Grant, Comput. Phys. Commun. **94**, 249 (1996).

[26] S. Fritzsche, J. Electron Spectrosc. Relat. Phenom. **114**, 1155 (2001).

[27] S. Fritzsche, Comput. Phys. Commun. **183**, 1525 (2012).

[28] S. Fritzsche, J. Nikkinen, S.-M. Huttula, H. Aksela, M. Huttula, and S. Aksela, Phys. Rev. A **75**, 012501 (2007).

[29] J. Viefhaus, G. Snell, R. Hentges, M. Wiedenhöft, F. Heiser, O. Geßner, and U. Becker, Phys. Rev. Lett. **80**, 1618 (1998).

[30] P. Lablanquie, F. Penent, R. I. Hall, H. Kjeldsen, J. H. D. Eland, A. Muehleisen, P. Pelicon, Z. Smit, M. Zitnik, and F. Koike, Phys. Rev. Lett. **84**, 47 (2000).

[31] P. Linusson, S. Fritzsche, J. H. D. Eland, L. Hedin, L. Karlsson, and R. Feifel, Phys. Rev. A **83**, 023424 (2011).

[32] J. Palaudoux, P. Lablanquie, L. Andric, K. Ito, E. Shigemasa, J. H. D. Eland, V. Jonauskas, S. Kučas, R. Karazija, and F. Penent, Phys. Rev. A **82**, 043419 (2010).

[33] Y. N. Joshi, J. Opt. Soc. Am. B **7**, 1182 (1990).

[34] F. Penent, P. Lablanquie, J. Palaudoux, L. Andric, G. Gamblin, Y. Hikosaka, K. Ito, and S. Carniato, Phys. Rev. Lett. **106**, 103002 (2011).